PHILOSOPHICAL TRANSACTIONS A

royalsocietypublishing.org/journal/rsta

Research

Cite this article: Auclair J-P, Dumont D, Lemieux J-F, Ritchie H. 2022 A model study of convergent dynamics in the marginal ice zone. *Phil. Trans. R. Soc. A* **380**: 20210261. https://doi.org/10.1098/rsta.2021.0261

Received: 16 March 2022
Accepted: 15 July 2022

One contribution of 17 to a theme issue 'Theory, modelling and observations of marginal ice zone dynamics: multidisciplinary perspectives and outlooks'.

Subject Areas:
oceanography, glaciology

Keywords:
marginal ice zone, modelling, ice strength, attenuation

Author for correspondence:
Jean-Pierre Auclair
e-mail: jean-pierre.auclair@univ-grenoble-alpes.fr

A model study of convergent dynamics in the marginal ice zone

Jean-Pierre Auclair[1,2], Dany Dumont[3], Jean-François Lemieux[4] and Hal Ritchie[4]

[1]Institut des Sciences de la Terre (ISTerre), CNRS/Université Grenoble-Alpes, Saint-Martin d'Hères, 38400, France
[2]Department of Oceanography, Dalhousie University, Halifax, Nova Scotia, B3H 4R2, Canada
[3]Institut des sciences de la mer de Rimouski, Université du Québec à Rimouski, Rimouski, Québec, G5L 3A1, Canada
[4]Recherche en Prévision Numérique environnementale, Environnement et changement climatique Canada, Dorval, Québec, H9P 1J3, Canada

J-PA, 0000-0002-7198-3185; DD, 0000-0003-4107-1799; J-FL, 0000-0003-2084-5759

With the increasing resolution of operational forecasting models, the marginal ice zone (MIZ), the area where waves and sea ice interact, can now be better represented. However, the proper mechanics of wave propagation and attenuation in ice, and especially their influence on sea ice dynamics, still remain poorly understood and constrained in models. Observations have shown exponential wave energy decrease with distance in sea ice, particularly strong at higher frequencies. Some of this energy is transferred to the ice, breaking it into smaller floes and weakening it, as well as exerting a stress on the ice similar to winds and currents. In this article, we present a one-dimensional, fully integrated wave and ice model that has been developed to test different parameterizations of wave–ice interactions. The response of the ice cover to the wind and wave radiative stresses is investigated for a variety of wind, wave and ice conditions at different scales. Results of sensitivity analyses reveal the complex interplay between wave attenuation and rheological parameters and suggest that the compressive strength of the MIZ may be better represented by a Mohr-Coulomb parameterization with a nonlinear dependence on thickness.

THE ROYAL SOCIETY PUBLISHING

This article is part of the theme issue 'Theory, modelling and observations of marginal ice zone dynamics: multidisciplinary perspectives and outlooks'.

1. Introduction

The marginal ice zone (MIZ) is defined as the region of the ice cover that is significantly impacted by surface ocean gravity waves [1]. The edges of both polar ice packs are the most commonly considered, although any area with seasonal sea ice cover is MIZ at some point, if not throughout the season. There, large waves coming from the open ocean can affect the ice over vast distances [2]. Waves can also provide a positive feedback to support the growth of polynyas [3]. In the context of a changing climate and particularly with a thinning sea ice cover [4], waves are also expected to play a larger role due to both an increase in available fetch and more fragile sea ice [5]. This can both impact climate simulations and, on a smaller scale, the accuracy of high-resolution sea ice forecasts that are particularly useful for navigation in the mid-latitude regions, where populations are higher and water use remains important even in the winter.

Wave attenuation in ice-covered seas has been studied for a long time. However, owing to the complexity of the environment and the difficulty of gathering data, no one all-encompassing attenuation model has emerged. Wadhams [6] suggested a creep model motivated by early attenuation measurements. Wadhams *et al.* [1] described the exponential decay of wave energy in sea ice using an empirical length scale that depends on wave frequency, ice floe size and ice thickness. Later, Kohout & Meylan [7] investigated further the scattering of waves by solid ice floes. The resulting wave phase resolving model simulation provides predictions of wave energy decrease in ice for a range of thickness and frequency that can be used to calculate attenuation. Various other attenuation models have also been suggested, with different ways to describe the ice or consider the underlying waves (e.g. [8–13]). Recent developments in technology and techniques are enabling new studies [14], and efforts are being made to discriminate between possible processes [11,15] and compare their effectiveness within a modelling setting [16,17].

Waves and ice interact in more ways than just the attenuation of wave energy. Waves can break up large floes into smaller, more mobile, ones (e.g. [2,18]), making the ice pack weaker when subjected to shear or compression. The broken ice floes can move more freely with respect to each other and the underlying ocean, and they thus enhance energy, mass and momentum fluxes across the ocean–ice–atmosphere interface [19]. As waves attenuate, the excess flow of momentum that they carry, also known as the radiation stress, varies in space and time, and a force is applied to the ice [20]. Stopa *et al.* [21] also showed how, around the Antarctic, waves can drive variability and, on average, contribute a force equivalent to the wind over 50 km. Wadhams [6] also hypothesized that this force may cause the formation of ice bands near the ice edge when wind-generated waves are reflected or absorbed by the upwind side of the band more strongly than the downwind side.

More recently, Williams *et al.* [22] studied the effect of wave-induced ice breakage and the radiation stress in a coupled wave–ice model. They found that waves can have a significant impact on the ice at scales of up to several tens of kilometres. In this impacted region, broken ice is more susceptible to wind forcing and also subjected to the wave radiation stress. Further from the ice edge, winds dominate over the ice dynamics. Sutherland & Dumont [23], using simultaneous *in situ* measurements of wave attenuation and ice thickness across the MIZ in the St Lawrence Estuary, Canada, were able to show that the radiation stress can be strong enough to thicken the ice through compression over distances that depend on the incident wave energy and the wave attenuation rate.

While the attenuation of waves by sea ice is present in some numerical wave models, the impact of waves on ice is missing in most operational ice models, and coupled models with two-way interactions are still fairly rare. In this study, a one-dimensional ice model is modified to incorporate waves and their interactions with ice. Particularly, the wave energy gradient caused

by wave attenuation in ice now applies a force on the ice through the radiation stress. Multiple parameterizations for wave attenuation, which in turn create different wave energy gradients in sea ice, are used along with different ice strength formulations to investigate the possible impact of this new wave stress on ice. The main contributions of this article are as follows: (1) a description of the evolution of sea ice when the wave radiation stress is considered, (2) the production of thickness and equilibrium energy profiles considering the radiation stress, to be tested against observations and (3) a presentation of the possible impact of the waves and ice strength on MIZ width, ice edge displacement and equilibrium ice thickness. In §2, the model used is described. Section 3 presents a case study of ice compression under wind and wave forcing with modifications to the wave attenuation and ice strength, while §4 presents the results of a sensitivity analysis, which are then discussed in §5.

2. Model description

The model used for this study is the one-dimensional viscous-plastic (VP) sea ice model described in the study by Auclair *et al.* [24], modified to add wave energy propagation and attenuation within the model as well as the force applied by the waves on sea ice. Because of the focus on short simulations and dynamics specifically, thermodynamics are not represented in the model. Both wind and wave forcing follow the same direction toward a closed boundary representing the shore. Waves originate from the other boundary, representing the offshore direction and propagate within the domain where they interact with the sea ice.

(a) Sea ice component

Because of the large difference between the vertical $\mathcal{O}(10^{-1} - 10^{1})$ m and horizontal $\mathcal{O}(10^{4} - 10^{6})$ m scales, sea ice dynamics is usually considered as a two-dimensional problem. The horizontal momentum balance is given by

$$\rho h \frac{D\mathbf{u}}{Dt} = -\rho h f \mathbf{k} \times \mathbf{u} + \boldsymbol{\tau}_a + \boldsymbol{\tau}_{wv} - \boldsymbol{\tau}_w + \nabla \cdot \boldsymbol{\sigma} - \rho h g \nabla H_d, \tag{2.1}$$

where ρ is the sea ice density, h is the mean ice thickness, $\mathbf{u}$ is the horizontal velocity vector of sea ice, f is the Coriolis parameter, $\mathbf{k}$ is a unit vector perpendicular to the horizontal plane, $\boldsymbol{\tau}_a$, $\boldsymbol{\tau}_{wv}$ and $\boldsymbol{\tau}_w$ are the wind, wave and water stresses, respectively, $\boldsymbol{\sigma}$ is the internal ice stress tensor, g is the gravitational acceleration and H_d is the sea surface height. Snow is neglected in this model.

Neglecting the Coriolis pseudo-force, the advection of ice momentum as done in [25] and [26] and the sea surface tilt due to the small scales considered, equation (2.1) can be simplified in one dimension to the following scalar equation:

$$\rho h \frac{\partial u}{\partial t} = \tau_a + \tau_{wv} - \tau_w + \frac{\partial \sigma}{\partial x}, \tag{2.2}$$

where u is the sea ice velocity component along the x-axis. As in [27], we assume that $v = 0$ and that y-derivatives are vanishing ($\partial \sigma_{xy}/\partial y = 0$) such that we can redefine $\sigma = \sigma_{xx}$ for simplicity. A derivation of the one-dimensional sea ice momentum equation is presented in [27].

Sea ice speed being much lower than wind speed, it is neglected in the wind stress term. Similarly, with the ocean being considered at rest, currents are neglected from the water stress term. Both formulations use quadratic drag formulas [28]:

$$\boldsymbol{\tau}_a = A \rho_a C_{da} |\mathbf{u}_a| u_a \tag{2.3}$$

and

$$\boldsymbol{\tau}_w = A \rho_w C_{dw} |\mathbf{u}| u, \tag{2.4}$$

where A is the sea ice concentration, ρ_a, ρ_w, $C_{da} = 1.2 \times 10^{-3}$ and $C_{dw} = 5.5 \times 10^{-3}$ are the densities and drag coefficients of air and water, respectively, and u_a is the surface wind. At low to mid concentrations, the space between floes can cause form drag (e.g. [29]) to be important.

However, due to the convergent nature of the experiments carried out in this study, concentration approaches 100% before thickening occurs and the focus is on the equilibrium thickness profile, and thus, form drag is neglected.

When waves hit and propagate in ice-covered seas, the horizontal momentum they transport is either absorbed or reflected and a force is exerted. Part of this force may be applied to the ice itself and part of it to the ocean. If the attenuation is dissipative, the momentum is transferred in the same direction, while if scattering happens, the momentum transfer can be higher as waves can be reflected in the opposite direction. This is called the wave radiation stress and can represent a significant forcing in the MIZ, as demonstrated by [23]. Here, we make two assumptions. First, all the stress goes to the ice primarily, since there is no evidence that it is otherwise and that if a stress applies to the ocean, it would drive a current under the ice that would reimpose a stress on the ice. Second, we assume that all the attenuation is dissipative at a scale larger than individual floes. When scattering happens, waves are scattered multiple times in all directions and are progressively and eventually dissipated. Given these assumptions, we follow the derivation of [23] and define the radiation stress per unit frequency $\tilde{\tau}_{wv}$ exerted by a wave spectrum $E_{wv}(x, f)$ along the wave propagation x-axis as follows:

$$\tilde{\tau}_{wv}(f) = -\rho_w g \frac{\partial}{\partial x}\left[E_{wv}(x, f)\left(2\frac{c_g(f)}{c_p(f)} - \frac{1}{2}\right)\right], \tag{2.5}$$

where c_p and c_g are the phase and group speeds, respectively, f is the wave frequency and ρ_w is the seawater density [23]. Integrating equation (2.5) over all the frequencies gives the total wave radiative stress exerted on the ice,

$$\tau_{wv} = \int_0^\infty \tilde{\tau}_{wv}(f)\,\mathrm{d}f, \tag{2.6}$$

or, for a discretized wave spectrum,

$$\tau_{wv} = \sum_{f_0}^{f_n} \tilde{\tau}_{wv}\,\Delta f. \tag{2.7}$$

Finally, the ice internal stress contribution to the momentum balance (2.2) is calculated from the divergence of the stress tensor as defined in [30]. In one dimension, since all other components vanish, it can be reduced to

$$\frac{\partial \sigma}{\partial x} = \frac{\partial}{\partial x}\left[(\eta + \zeta)\frac{\partial u}{\partial x} - \frac{P}{2}\right], \tag{2.8}$$

where ζ and η are the bulk and shear viscosities, respectively, and P is a pressure-like term, which is a function of the ice strength and of the strain rates. Viscous coefficients are defined as follows:

$$\zeta = \frac{P_p}{2\Delta} \tag{2.9}$$

and

$$\eta = \zeta\, \mathrm{e}^{-2}, \tag{2.10}$$

where P_p is the ice strength, e is the aspect ratio of the elliptical yield curve [30] and Δ is a nonlinear function of the one-dimensional deformation rate:

$$\Delta = \left[(1 + \mathrm{e}^{-2})\left(\left(\frac{\partial u}{\partial x}\right)^2 + \epsilon_2\right)\right]^{1/2}. \tag{2.11}$$

Here, $\epsilon_2 = 10^{-22}\ \mathrm{s}^{-2}$ is a small number used to prevent cases, where $\Delta = 0$ in computations of ζ.

Following [30], ζ is capped to a maximum value, which characterizes the viscous regime. To maintain a continuous derivative, this is done using a hyperbolic tangent as in [31]:

$$\zeta = \frac{P_p}{2\Delta_{\min}} \tanh\left(\frac{\Delta_{\min}}{\Delta}\right), \tag{2.12}$$

with $\Delta_{\min} = 2 \times 10^{-9}\ \mathrm{s}^{-1}$ in accordance with the $\zeta_{\max}$ definition in [30]. Finally, to prevent the development of ice drift in the absence of forcing [32], we use a replacement closure to define P

as follows:

$$P = 2\zeta\,\Delta. \tag{2.13}$$

In his seminal paper, Hibler [30] defined the ice strength P_p as follows:

$$P_{\text{Hibler}} = P^* h\, \mathrm{e}^{-C(1-A)}, \tag{2.14}$$

where P^* and C are the strength and concentration parameters, respectively. This formulation has been widely adopted and applied to represent compact ice conditions of the inner ice pack in large-scale ice models. In the MIZ, where sea ice is usually fragmented in small pieces (floes) that heave, tilt and surge in response to waves, ice thickens homogeneously as a result of floe rafting and brash convergence instead of breaking at localized ridging lines [23]. For such cases, a Mohr-Coulomb formulation developed for river ice jumbles [33] provides an appropriate description of the MIZ dynamics. Sutherland & Dumont [23] also found good agreement between ice thickness profiles calculated by equating the Mohr-Coulomb ice strength with wave radiation stress and *in situ* measurement of ice thickness compressed by waves in a MIZ of the St Lawrence Estuary.

In the Mohr-Coulomb model, the ice compressive strength (P_p, hence P_{MC} for the Mohr-Coulomb formulation) represents the work against gravity and buoyancy required to increase the ice thickness through both ridging and rafting as opposed to the ice's material strength. By using this model, Dai *et al.* [34] defined the ice strength as follows:

$$P_{\text{MC}} = K_r h^2, \tag{2.15}$$

with

$$K_r = \frac{\rho g}{2}\left(1 - \frac{\rho}{\rho_w}\right)(1-n)\left(\frac{1+\sin\phi}{1-\sin\phi}\right), \tag{2.16}$$

where n is the ice porosity and ϕ is the internal friction angle. We note here that the compressive strength has a quadratic dependence on h instead of a linear dependence in the ice strength as defined in [30], P_p in equation (2.14) (now referred to as P_{Hibler}), to represent compact ice conditions of the inner ice pack in large-scale ice models. However, the quadratic model may predict unreasonably large compressive strength for thicker ice.

To blend the two formulations in a way that allows our model to apply to a broad range of thickness values, a hybrid strength with an additional dependence on thickness added to equation (2.14) was tested, defined by

$$P_{\text{hybrid}} = P^* h \tanh(\gamma h)\, \mathrm{e}^{-C(1-A)}, \tag{2.17}$$

where γ is an adjustable parameter that controls the transition between the two regimes. This modification is motivated by the fact that for small values, the hyperbolic tangent varies similarly to its argument, while it plateaus to 1 for large values, allowing this formula to approximate a quadratic dependence on thickness at low thickness, and a linear one at larger thickness. It is similar in spirit to the modification introduced by Chikhar *et al.* [35] to better match observed sea ice drift in the Arctic after introducing a parameterization for form drag. However, this formulation tends to two physical regimes and orders of dependency at its extremes while still allowing a smooth, differentiable transition, unlike a piece-wise quadratic-linear formula linking the two at some thickness.

Figure 1 shows the thickness dependence of the Hibler and Mohr-Coulomb compressive strength formulations as well as the blended formulation for two values of γ, 1/2 and 1/4. For P_{Hibler}, a typical P^* value of 27.5 kPa was chosen for the curve, with the shaded area representing the range of values from the literature from 10.8 to 48.8 kPa. For P_{MC}, typical values of $n = 0.4$ and $\phi = 34^\circ$ were chosen for the curve and the shaded areas represent the range from porous, easy to stack ice with $n = 0.5$ and $\phi = 26^\circ$ to denser ice with $n = 0.5$ and $\phi = 58^\circ$. This hybrid ice strength was chosen so that it increases quadratically for thin ice. As ice thickness increases, the hyperbolic tangent approaches 1 and the ice strength approaches the P_{Hibler} values to better represent the two failure types in sea ice.

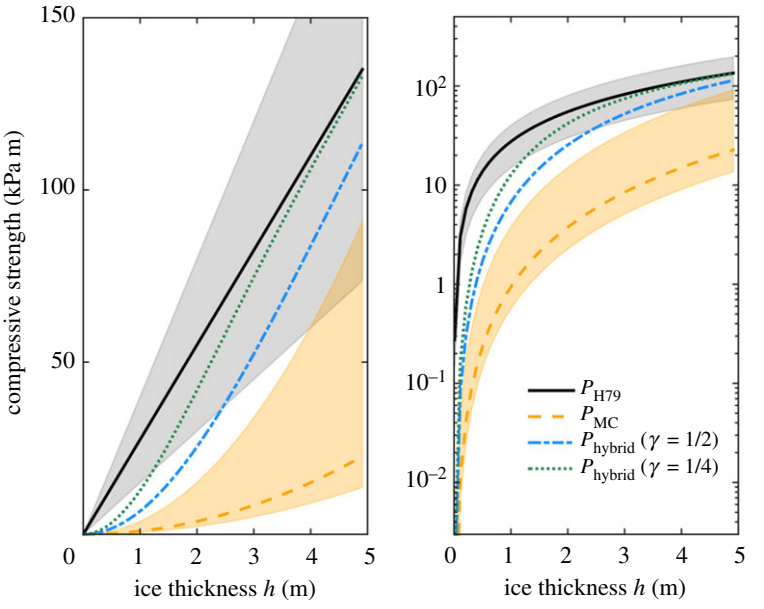

Figure 1. Parameterizations of ice compressive strength as a function of ice thickness in linear (left) and logarithmic (right) scales: P_{H79} refers to equation (2.14) (black solid line), P_{MC} to equation (2.15) (yellow dashed line) and P_{hybrid} to equation (2.13) for $\gamma = 1/2$ (blue dash-dotted line) and $\gamma = 1/4$ (green dotted line). Shaded areas represent the range of possible values found in the literature. (Online version in colour.)

(b) Wave component

Surface gravity waves, defined as a frequency-dependent spectrum at the offshore boundary, propagate inside the domain using a one-dimensional version of the advection–attenuation equation (equation (2.18)). At each time step, the wave energy spectrum, E_{wv}, is advected and attenuated by the sea ice (S_{ice}):

$$\frac{\partial E_{wv}}{\partial t} + c_g \frac{\partial E_{wv}}{\partial x} = S_{ice}. \tag{2.18}$$

Energy advection is done using the group velocity ($c_g = \partial\omega/\partial k$) calculated for each frequency bin and location, using the ice thickness at that location. As we are considering the very edge of the ice, where floes tend be smaller than the peak wavelength, the mass loading wave dispersion relation is used [36], i.e.

$$\omega^2 = gk\left[\frac{\rho}{\rho_w} kh + \coth(kd)\right]^{-1}, \tag{2.19}$$

where $\omega = 2\pi f$ and d is the water depth. Since the purpose of the model is to study the interaction with specified spectra, the wave energy spectrum does not change except for the diffusion caused by the frequency dependence of the group velocity and the attenuation caused by sea ice.

(i) Wave attenuation

Wave energy is attenuated by the presence of ice. It results from the scattering of waves by individual ice floes, from the dissipation of energy through a number of processes such as turbulence, wave-induced break-up and floe-floe friction, and possibly from other nonlinear wave–wave or wind–wave or wave–current interactions. Wave attenuation is thus a complex multivariate problem, and there is currently no single model that generally applies to the MIZ. In this study, we use two existing and very contrasting attenuation models to explore how the magnitude and dependence of wave attenuation on wave frequency and ice thickness affect the push on the ice and its dynamical response. The first model is purely based on conservative scattering of waves by ice floes and the assumption that the observed attenuation results from

the progressively decreasing transmitted wave energy within the MIZ made of individual ice floes [7]. The second model is a two-layer semi-permeable representation of the ice cover where wave energy is dissipated by viscous losses [12]. The two models are meant to represent possible yet contrasting attenuation functions, in terms of form and magnitude, that could apply to the MIZ, to study the sensitivity of its response to waves.

The ice interaction source term S_{ice} describes an exponential decay within the ice:

$$S_{\text{ice}} = -\beta(A,h,f)\, E_{wv}, \tag{2.20}$$

where β is a temporal attenuation coefficient (s^{-1}). The model of Kohout & Meylan [7] simulate the scattering of monochromatic waves as they encounter ice floes for a range of thicknesses and frequencies to obtain α, a spatial attenuation coefficient (m^{-1}). The two coefficients α and β are related by

$$\beta = \alpha c_g. \tag{2.21}$$

As this is a spectral model and waves are not individually resolved, look-up tables built from the simulations in [7] are used to recover the α values.

In the study by Sutherland *et al.*'s model [12], the temporal attenuation coefficient is defined as follows:

$$\beta = \frac{\nu\omega^2\Delta_0}{2g\epsilon h}, \tag{2.22}$$

where

$$\nu = \frac{1}{2}\epsilon^2\omega h^2, \tag{2.23}$$

and ϵ is the relative thickness of a permeable layer in the ice cover and Δ_0 is a parameter related to the amplitude of wave motions within that permeable layer, both between 0 and 1. Combining the two, we obtain the temporal attenuation coefficient used in equation (2.20) as a function of frequency and thickness:

$$\beta = \frac{\epsilon\Delta_0 h\omega^3}{4g}, \tag{2.24}$$

with two free parameters, ϵ and Δ_0, both bounded by between 0 and 1. Here, we choose a value of 0.5 for the product $\epsilon\Delta_0$, consistent with the analysis of [12] of three datasets where both wave parameters and ice thickness estimates were available.

Alternatively, the model can use attenuation rates per floe, a, from [7]. These are converted to an attenuation rate per unit distance using $\alpha = Aa/D$, where D is the floe diameter. Since the model does not directly simulate floe size and given the requirement for large floe size for the calculation of the attenuation coefficient, a fixed floe size of 10 m was used in the simulations, chosen as a representative value for the floes observed during the field study of [23]. With the scattering model, attenuation increases as the floe size decreases since more scattering events occur, while the two-layer attenuation does not depend on floe size. This spatial attenuation is then converted to the temporal attenuation rate, β, with equation (2.21), and used in equation (2.20).

The attenuation coefficients (α_{KM08}) obtained from [7] are generally weaker than the ones (α_{S19}) calculated using the fitted solutions of [12], as shown in figure 2. The most important differences between the two attenuation schemes is that α_{KM08} is much lower at low frequencies and small thicknesses and that it has a weaker dependence to thickness at low frequencies. However, the difference in attenuation coefficients at high frequency and large thickness is less meaningful since in a typical thickness profile increasing from the ice edge to the shore, high-frequency waves will have been attenuated by thinner ice before encountering the thick ice.

(c) Numerical scheme

A backward Euler scheme is used for the sea ice momentum equation, as in [24]. Once the ice velocity solution is found, advection of ice thickness, concentration and wave energy along

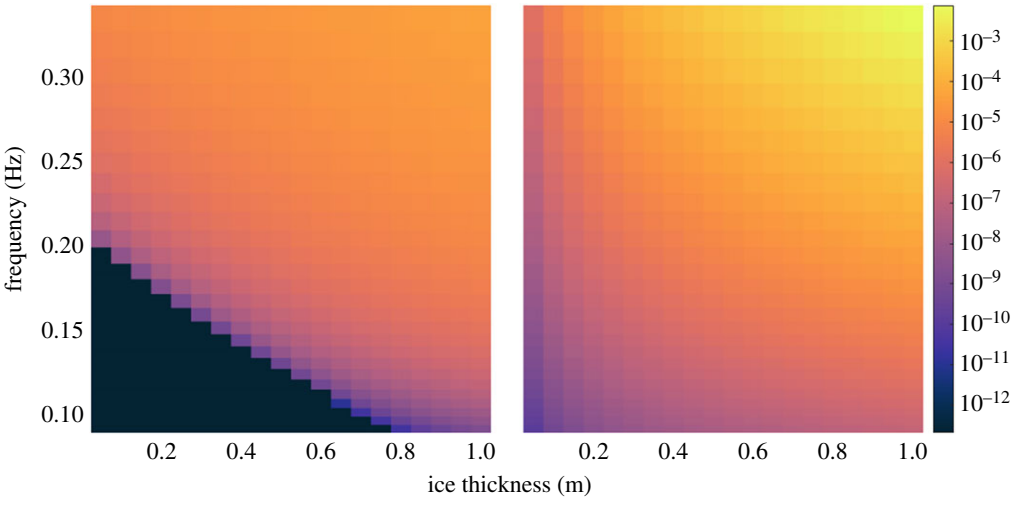

Figure 2. Wave attenuation coefficient α in m^{-1} as a function of wave frequency f and ice thickness h as computed from [7] (α_{KM08}, left panel) and from [12] (α_{S19}, right panel). (Online version in colour.)

with the attenuation of wave energy attenuation are performed to complete the time step. The continuity equations of the ice thickness and the ice concentration as well as the wave advection and attenuation equations are solved explicitly with a forward Euler scheme.

The time-discretized sea ice momentum equation in one dimension is written as follows:

$$\rho h^{n-1}\frac{(u^n - u^{n-1})}{\Delta t} = \tau_a^n + \tau_{wv}^n - \tau_w^n + \frac{\partial \sigma^n}{\partial x}, \tag{2.25}$$

where the superscript n denotes the current time level, and $n-1$ is the previous, known, time level. We use a one-thickness category model. Equation (2.25) is solved using a Jacobian-free version of Newton's method. At every iteration of Newton's method, the dispersion relation equation (2.19) for waves in sea ice is solved for every frequency and location. The wave energy is then advected and attenuated using equation (2.18), and the energy gradient is used to calculate the wave stress (equation (2.7)) on the ice. With all the stresses, the ice velocity u^n is found by the implicit solver. The continuity equations for both concentration, A, and mean thickness, h, are then solved explicitly:

$$\frac{(A^n - A^{n-1})}{\Delta t} + \frac{\partial}{\partial x}(u^n A^{n-1}) = 0 \tag{2.26}$$

and

$$\frac{(h^n - h^{n-1})}{\Delta t} + \frac{\partial}{\partial x}(u^n h^{n-1}) = 0. \tag{2.27}$$

With this formulation, the mean thickness is defined over the entirety of a grid cell, with open water counting as having zero thickness. The thickness of the ice itself within a grid cell, identified as floe thickness herein, is considered uniform and can then be retrieved by dividing the mean thickness by the concentration. Given the present focus on convergence, concentrations tend to be close to 1 and mean thickness close to floe thickness.

Spatially, the model uses a staggered grid where ice concentration, thickness and wave energy are collocated, and both ice and wave velocities are defined in between tracer points, in a one-dimensional version of the Arakawa C-grid [37]. The model has one closed boundary where homogeneous Dirichlet boundary conditions are applied ($u = 0$), toward which the wind and waves push the ice, representing the shore. The other boundary is open, with constant wave forcing and open waters, representing the offshore direction. Spatial derivatives are discretized using a second-order centred difference scheme. For a number of tracer points nx, the discretization of the momentum equation creates a system of $nx + 1$ equations.

Waves and all the associated variables are defined in the model at ice tracer points and the numerical scheme follows that of [9]. At every time level, wave properties are calculated from the newly advected ice properties. Because of the difference in time scale between advection and attenuation in the problem, the wave energy is advected first and then attenuated. Advection is performed using a Lax–Wendroff scheme [38] with Superbee flux limiter [39]. First, the energy difference between neighbouring grid cells is calculated. By using these differences, two parameters are calculated as follows:

$$\theta(x, f) = \frac{E(x, f) - E(x - \Delta x, f)}{E(x + \Delta x, f) - E(x, f)} \tag{2.28}$$

and

$$\phi(x, f) = \begin{cases} 0 & \theta(x, f) \leq 0 \\ 2\theta(x, f) & 0 < \theta(x, f) \leq 0.5 \\ 1 & 0.5 < \theta(x, f) \leq 1 \\ \theta(x, f) & 1 < \theta(x, f). \end{cases} \tag{2.29}$$

By using these two parameters, the flux is defined as follows:

$$F(x, f) = E(x, f) + \frac{\phi(x, f)}{2}\left(1 - c_g(x, f)\frac{\Delta t}{\Delta x}\right)(E(x + \Delta x, f) - E(x, f)). \tag{2.30}$$

With the fluxes calculated, the advected energy is calculated as follows:

$$E^n_{\text{adv}}(x, f) = E^{n-1}(x, f) - c_g(x, f)\frac{\Delta t}{\Delta x}(F^{n-1}(x, f) - F^{n-1}(x - \Delta x, f)). \tag{2.31}$$

The attenuation of waves due to the ice is calculated on the advected energy (E^{n+1}_{adv}) using the temporal attenuation coefficients defined in §2b(i) in an analytic solution to the wave attenuation equation:

$$E^{n+1}(x, f) = E^{n+1}_{\text{adv}}(x, f)e^{-\beta(x, f)\Delta t}. \tag{2.32}$$

To operate seamlessly, both the wave and the sea ice components of the model use the same time step. While this significantly decreases the possible time step of the sea ice model due to the high velocity of the waves, it also ensures that waves and ice evolve in unison. The smaller time step also has the advantage of improving the quality of the initial guess provided to the implicit solver used for the sea ice velocities and helping numerical convergence.

3. Case study

To test the model described earlier, simulations were performed on a 40 km domain using a 250 m resolution and 5 s time step. This domain size was chosen as it enabled simulations to represent well the wave-dominated regime of the experiment without spending too much effort modelling the strictly wind-dominated regime that has been described previously [24,40,41]. An initially uniform 70% concentration and 10 cm thick ice cover were subjected to 10 m s^{-1} winds. Waves represented by a JONSWAP spectrum [42] corresponding to the wind speed [43] used are also generated at the offshore boundary and propagate towards the ice.

The reference, P_{Hibler}, ice strength was used along with two versions of the hybrid (P_{hybrid}) formulations 2.17, with factors γ of 1/2 and 1/4. Wave attenuation was calculated using either the formulation of Kohout & Meylan [7] or the one from Sutherland *et al.* [12], as described earlier. Attenuation in both parameterizations occurs mostly near the ice edge (figure 3). The main difference is stronger attenuation even in thin ice in the formulation by Sutherland *et al.* [12]. This strong local energy gradient applies a larger force at the ice edge following equation (2.5).

The sea ice thickness evolution shows the large impact of using the hybrid formulation when dealing with thin ice. Ice edge movement and final thickness obtained using both of the γ factors are noticeably different from the results from the VP simulations using P_{Hibler} (figure 4), regardless of the attenuation function used.

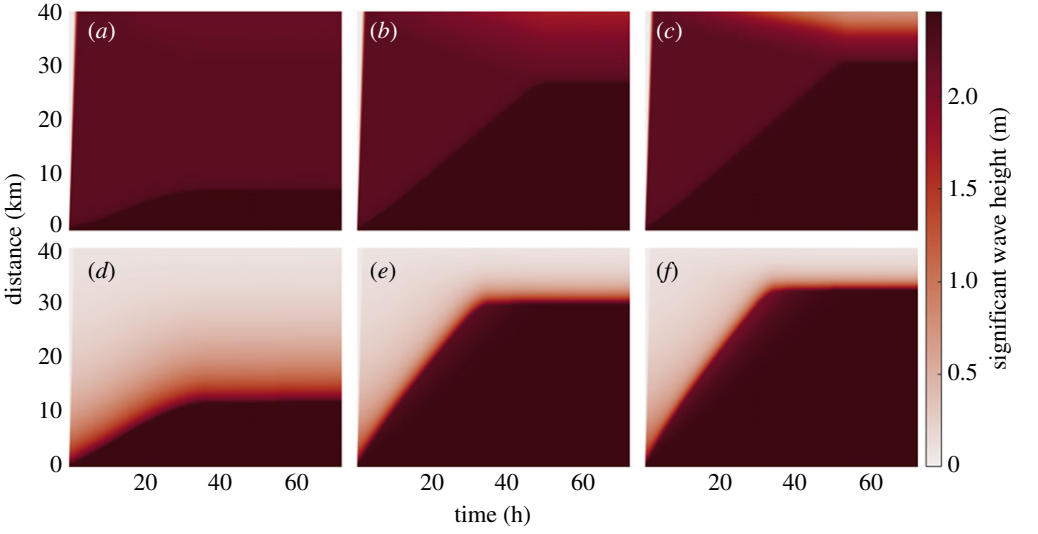

Figure 3. Time evolution of significant wave height H_s along a 40-km transect from the open ocean (bottom) to the coast (top), for different parameterizations of compressive ice strength and wave attenuation: P_{H79} (*a*,*d*), P_{hybrid} with $\gamma = 1/2$ (*b*,*e*), P_{hybrid} with $\gamma = 1/4$ (*c*,*f*), α_{KM08} (*a*,*b*,*c*) and α_{S19} (*d*,*e*,*f*). (Online version in colour.)

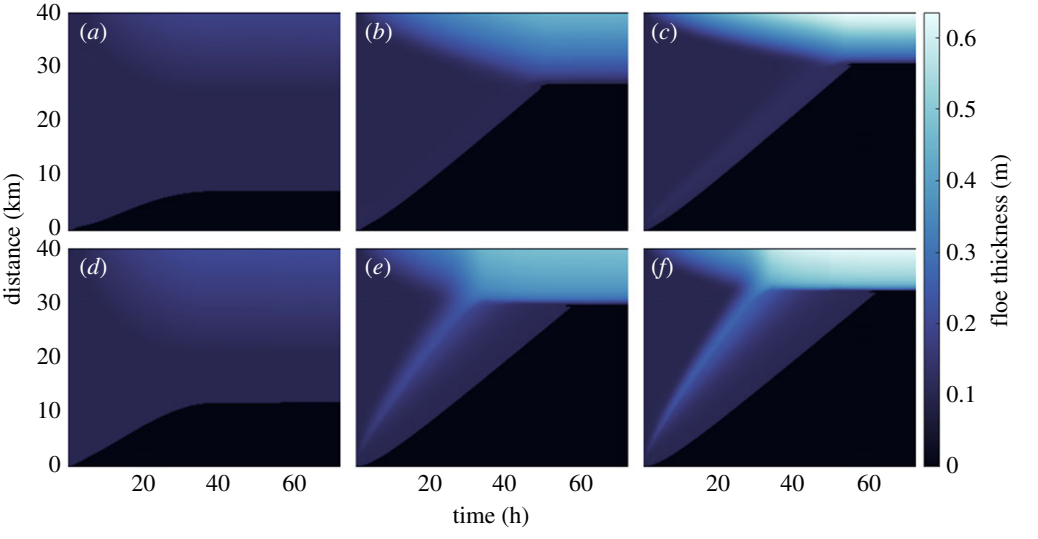

Figure 4. Time evolution of ice thickness along a 40-km transect from the open ocean (bottom) to the coast (top), for different parameterizations of compressive ice strength and wave attenuation: P_{H79} (*a*,*d*), P_{hybrid} with $\gamma = 1/2$ (*b*,*e*), P_{hybrid} with $\gamma = 1/4$ (*c*,*f*), α_{KM08} (*a*,*b*,*c*) and α_{S19} (*d*,*e*,*f*). (Online version in colour.)

Between the two wave attenuation parameterizations used, two differences also emerge. First, compression occurs in two areas when using Sutherland *et al.*'s [12] attenuation in the weakened ice: not only at the shore but also in a thin area further offshore where the wave stress is locally the strongest, visible as a thin diagonal line going from the offshore boundary early in the simulation towards the compressed ice pack later. Second, once the ice has reached an equilibrium with the forcing after 60 hours, the thickness profile is much sharper for Sutherland *et al.*'s [12] attenuation due to its stronger attenuation for small thicknesses, as visible in figure 5 showing thickness

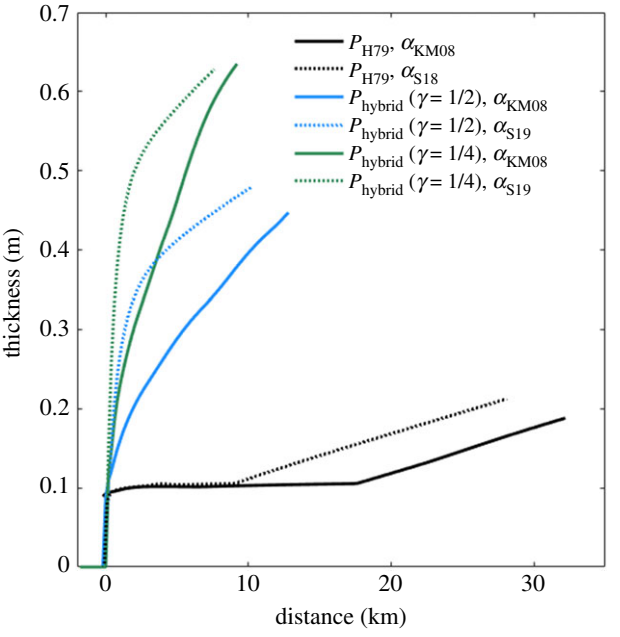

Figure 5. Sea ice thickness as a function of distance from the ice edge after 72 hours, at equilibrium, for different parameterizations of compressive ice strength and wave attenuation. (Online version in colour.)

profiles at a given distance from the ice edge. However, the final equilibrium thicknesses at the closed, shore boundary are similar between the two formulations.

The difference in attenuation coefficient changes the sea ice dynamics significantly near the ice edge. To assess the impact of waves in the ice dynamics, the total force exerted by both waves and winds was calculated by integrating the stress terms from equation (2.2) starting at the ice edge. This method allows us to consider not only the local stress exerted but also the stress transmitted by internal ice stresses. The difference between these two terms, as shown in figure 6, can be used to determine where waves dominate over the wind in the ice dynamics, which could be used to define a dynamical MIZ, in complement to the other typical definition such as a concentration of 15% or the dominance of ice fragmented by waves.

The stronger attenuation predicted by the fitted Sutherland *et al.*'s [12] parameterization (figure 6, bottom) creates much larger stresses, the influence of which is felt much further in the ice, creating a dynamical MIZ around three times as wide. Interestingly, for the weakest ice modelled (figure 6, right), the thickening of ice at the closed, shore boundary allows attenuation of longer wave periods than what has been attenuated at the ice edge. This additional inshore wave stress causes further thickening and a dynamical MIZ width that is similar between the two attenuation methods, unlike the other two ice strength parameterizations.

4. Modelled wave impact on ice

To assess the possible effect of including wave forcing in sea ice models, multiple model runs were performed for a range of wind speeds and initial ice thicknesses using both the P_{Hibler} and P_{Hybrid} ice strength as well as the attenuation formulations by [7,12]. Initial conditions and wind forcing were uniform over the 80 km domain, with wave forcing coming from a constant spectrum propagating from the offshore boundary of the domain. Reference simulations were also run without waves. All simulations were performed for 4 days. This time was sufficient for the sea ice to reach a thickness where it can sustain the forcing from winds and waves combined, entering a steady-state solution. Three parameters were chosen as the most descriptive of the

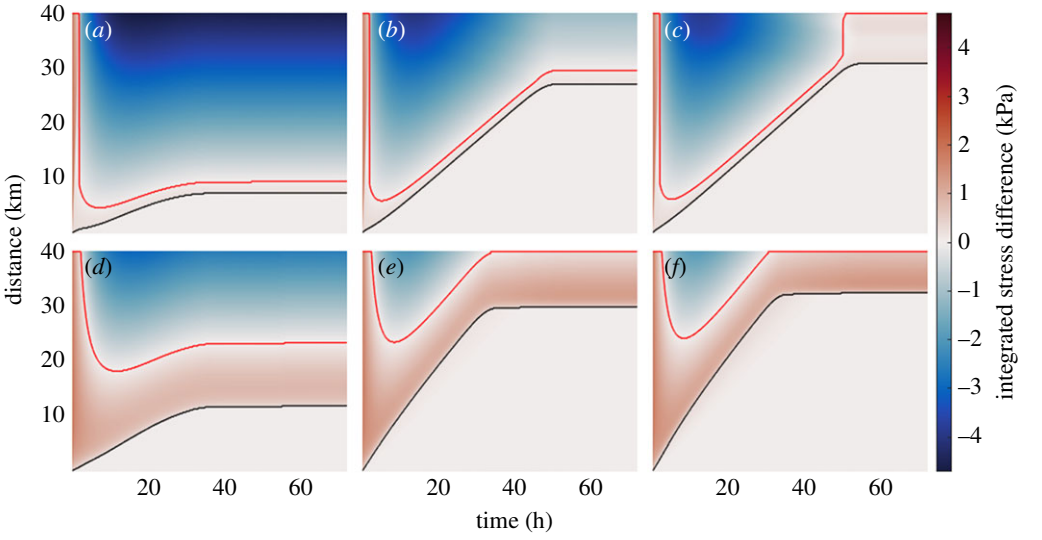

Figure 6. Time evolution of the integrated wave and wind stress difference along a 40-km transect from the open ocean (bottom) to the coast (top), for different parameterizations of compressive ice strength and wave attenuation: P_{H79} (*a*,*d*), P_{hybrid} with $\gamma = 1/2$ (*b*,*e*), P_{hybrid} with $\gamma = 1/4$ (*c*,*f*), α_{KM08} (a–α_{S19} (*d*–*f*). The black and red curves represent the ice edge and the locations where integrated wave and ice stresses are equal. (Online version in colour.)

impact of having waves in the simulation: the displacement of the ice edge, the width of the MIZ defined as the distance over which integrated wave stresses are larger than integrated wind stresses, as in the previous section, and the sea ice thickness at the shore-ward end of the MIZ.

The location of the boundary between open and ice-infested waters is a critical forecast variable. The presence or absence of ice is key to navigation planning and waves can apply a large force right at the edge, moving it rapidly in their direction of propagation. In this case, we consider the ice edge to be the location where ice concentration in the model goes above 30%, as the traditional 15% threshold was crossed at negligible sea ice thicknesses in some simulations of the sensitivity study and blurred the measurements in comparison of MIZ width. Results shown in figure 7 present the effect of winds alone (top row) as well and the combined effect of winds and waves. In all cases, ice edge displacement increases with wind speeds and decreases with initial ice thickness. Even though the waves are essentially completely attenuated by the ice using both models, the Sutherland *et al.*'s [12] attenuation formulation increases the displacement by creating a stronger energy gradient, which is more effective at converting wave energy into a force on the ice. Weakening the ice through the hybrid formulation also increases displacement, but has more of an impact at low starting thicknesses.

Subtracting the displacement obtained in the reference, wind only, model runs from the runs with waves, and the impact of adding waves can be seen to reach up to 20–25 km in figure 8. The impact of the choice of attenuation model also becomes much more apparent. On average, the Sutherland *et al.*'s [12] attenuation model displaces the edge by 5 km more in weaker ice. In the case of Hibler's strength formulation, a difference in displacement of up to 15 km can be seen due to the ice remaining thin, a range where the two formulations differ significantly.

The dynamical MIZ, defined as the region where the local applied force on the ice, or the integral of stresses from the ice edge, is dominated by waves, provides information on the scale of modelling where considering waves will be important. As shown in figure 9, the width of the MIZ tends to increase with wind speed. Wave energy and thus wave stress have a fourth-order dependence on wind speed, while wind stress depends on wind speed quadratically. Longer fetches on ice are necessary for the wind stress to catch up to the stronger wave stress in terms of applied force, leading to the wider dynamical MIZ. The two attenuation formulations

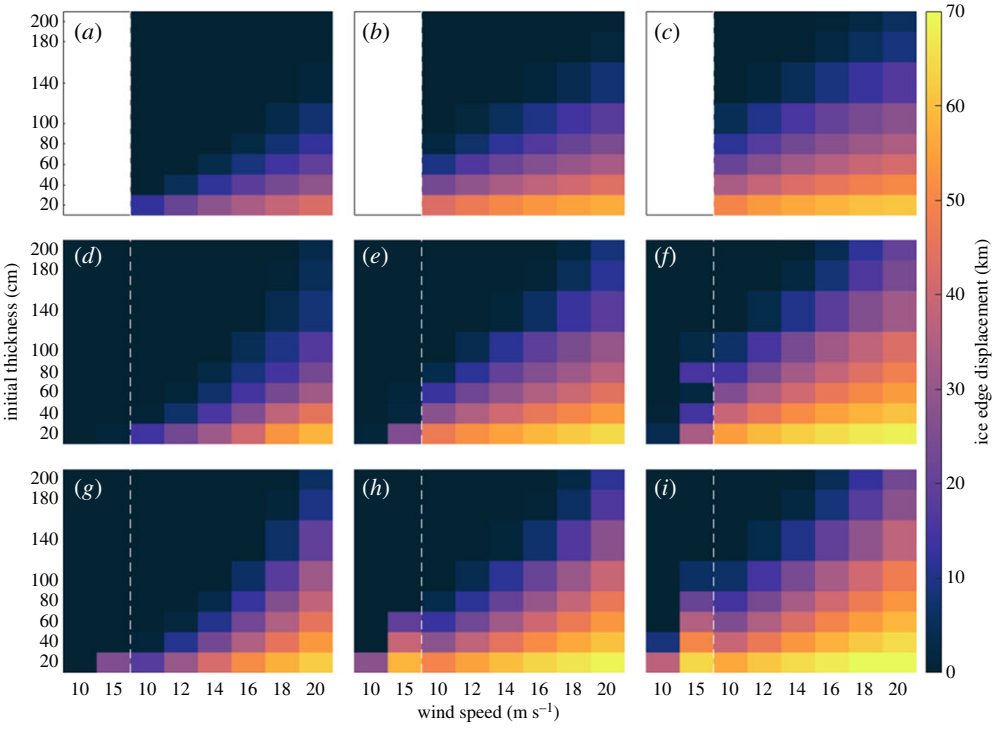

Figure 7. Ice edge displacement from its original position at $x = 0$ as a function of wind and/or wave forcings and initial uniform thickness, for different attenuation and strength parameterizations. The first column (*a*,*d*,*g*) uses P_{H79}, the second column (*b*,*e*,*h*) uses P_{hybrid} ($\gamma = 1/2$) and the third column (*c*,*f*,*i*) uses P_{hybrid} ($\gamma = 1/4$). The top row (*a*,*b*,*c*) shows results with wind forcing only, while the second and third rows are forced with winds and waves using the wave attenuation parameterizations α_{KM08} (*d*,*e*,*f*) and α_{S19} (*g*,*h*,*i*), respectively. Results to the left of the white dashed line are forced with waves only, corresponding to indicated wind speed values. (Online version in colour.)

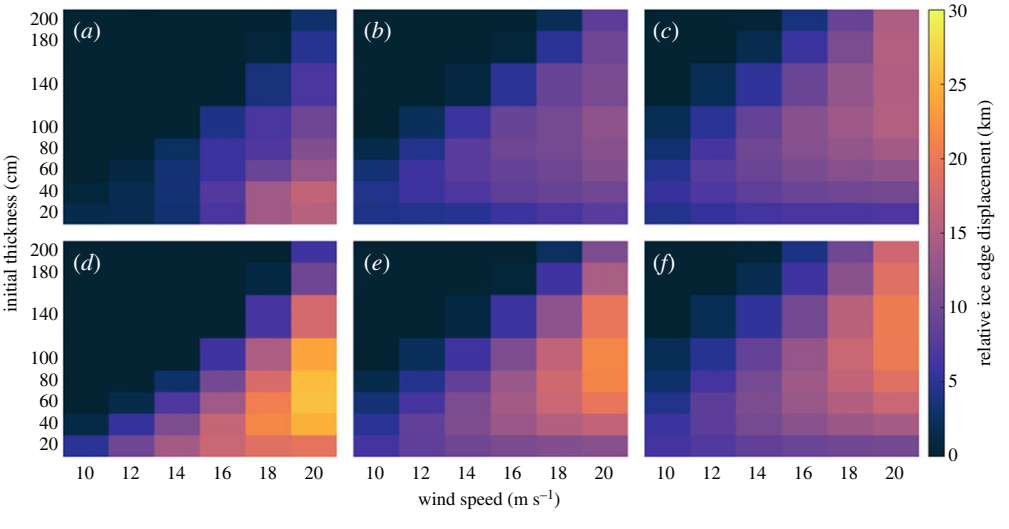

Figure 8. Ice edge displacement in kilometres, relative to the location in equivalent wave-free simulations, for wind speeds of 10 to 20 m s^{-1} and initial uniform ice thickness of 20–200 cm, for different attenuation and strength parameterizations: P_{H79} (*a*,*d*), P_{hybrid} ($\gamma = 1/2$) (*b*,*e*), P_{hybrid} ($\gamma = 1/4$) (*c*,*f*) and attenuation α_{KM08} (*a*,*b*,*c*) and α_{S19} (*d*,*e*,*f*). (Online version in colour.)

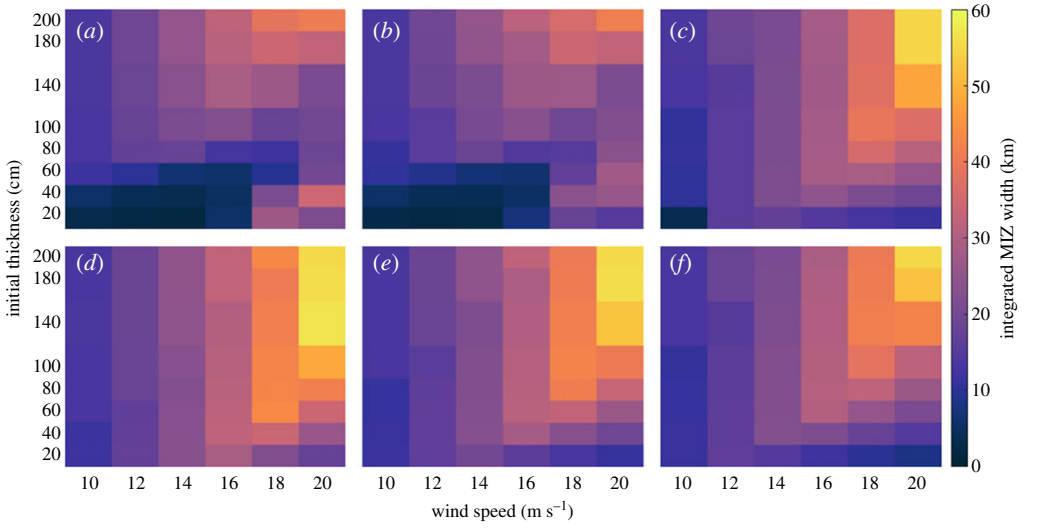

Figure 9. MIZ width in kilometres, measured by comparing integrated wind and wave stresses, for wind speeds of 10 to 20 m s^{-1} and initial uniform ice thickness of 20–200 cm, for different attenuation and strength parameterizations: P_{H79} (*a*,*d*), P_{hybrid} ($\gamma = 1/2$) (*b*,*e*), P_{hybrid} ($\gamma = 1/4$) (*c*,*f*), attenuation α_{KM08} (*a*,*b*,*c*) and α_{S19} (*d*,*e*,*f*). (Online version in colour.)

differ significantly in the shape of this dependence on initial thickness. With the formulation by Kohout & Meylan [7], there are two different regimes. At low initial thickness, waves are attenuated only when the wind is strong enough to first compact the ice to a thickness where it can attenuate waves, leading to a local maximum at high winds and low thickness. In this case, wave attenuation occurs near the shore. At higher initial thickness, the ice is able to attenuate waves closer to the ice edge. In between the two regimes, a local minimum in MIZ width as a function of thickness is attained when the ice can resist the winds but is not thick enough to attenuate waves. The Sutherland *et al.*'s [12] attenuation formulation, having stronger attenuation for low thickness, does not show the two regimes and attenuation is always greatest near the ice edge. In both attenuation formulations, the first increase of MIZ width with initial ice thickness is due to the dynamical MIZ extending to the shore boundary of the domain. The decrease in ice edge displacement as initial thickness increases leaves more of the model domain available to the MIZ. With a larger domain, the dynamic MIZ width would not show this dependence.

For the given wind speed and ice concentration values, the local wind stress on ice is the same at every location. This value is much smaller than the peak wave stress. This allows thin ice to resist the local force near the ice edge if waves are not considered. Waves, by exerting stress at or near the ice edge, create a much sharper increase in thickness in that area. The ice thickness at the point where wind and wave forces are equal, or equilibrium thickness shown in figure 10, gives a measure of the effect of waves depending on conditions. For the typical VP ice strength, waves are insufficient to compact even 20 cm ice up to wind speeds of 16 to 18 m s^{-1}. Weakening the ice using the hybrid formulation allows waves associated with weaker winds to compact it. For a given wind speed, there is a specific minimum ice thickness that will be able to balance it. Any initial ice thickness below that value will be compacted to that thickness, leading to the equilibrium thickness being independent of the initial value or vertical bands in the figure. Past that value, the ice is already strong enough to sustain the forces and will not be thickened, seen as horizontal bands in the figure. Both attenuation models reach similar values for the weakest ice where compaction enables thickening and stronger attenuation by the Kohout & Meylan [7] formulation. Results differ for stronger ice where the thickness–attenuation–compaction feedback is more dependent on wave attenuation at low thicknesses. Similar to the MIZ width, the decrease in thickness associated with low initial thickness is due to the model domain truncating the MIZ.

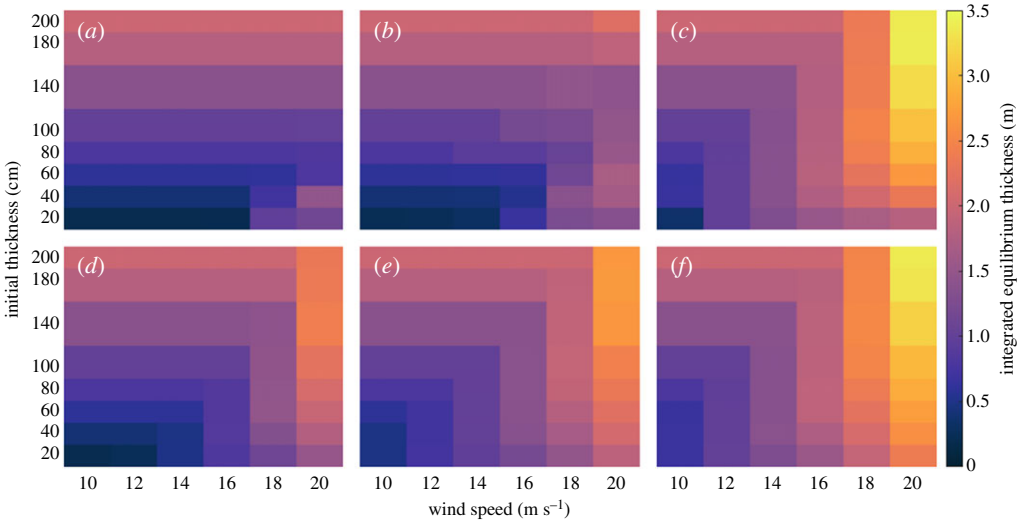

Figure 10. Ice thickness at the point where integrated wind and wave stresses are equal to each other, for wind speeds of 10 to 20 m s^{-1} and initial uniform ice thickness of 20–200 cm, for different attenuation and strength parameterizations: P_{H79} (*a*,*d*), P_{hybrid} ($\gamma = 1/2$) (*b*,*e*), P_{hybrid} ($\gamma = 1/4$) (*c*,*f*) and attenuation α_{KM08} (*a*,*b*,*c*) and α_{S19} (*d*,*e*,*f*). (Online version in colour.)

5. Discussion and conclusion

By using a one-dimensional wave–ice model, it was possible to reproduce key mechanisms of wave–ice interactions in the MIZ. Simulations showed how dependent those features are on a complex balance of forces, most of which are still not well understood. By looking into which combinations of formulations reach an appropriate balance, insight into what might actually be happening in the MIZ can be gained.

The numerical experiments presented earlier demonstrated how the ice strength formulation that is the most commonly used for modelling sea ice at large scales, Hibler's formulation, fails when applied to the MIZ. This is of little surprise as, in the ice pack, convergence produces highly localized ridging, whereas in the MIZ, thickening happens everywhere mostly through floe rafting. This evolution is facilitated by the wave motion and the small size of ice fragments. In our study, the greater ease of compaction is represented by a formulation that has a lower ice strength for thin ice, as it is expected to be more fragmented and more easily agitated by waves. In the MIZ, ice strength parameterizations should ideally account directly for the effect of waves in facilitating rafting. For example, considering the ratio of ice thickness to wave height as a first-order parameter would likely provide a more physically grounded and versatile formulation.

Models for wave attenuation currently abound, all for a specific set of circumstances but applied widely to all cases. As was the case in this study, changing formulations can have a wide range of effects. Particularly, the magnitude and localization of the wave radiation stress applied on the ice were observed to depend strongly on the strength of wave attenuation, creating a feedback that could change ice thickness by a factor of two or more. Indeed, stronger attenuation not only extracts more energy from the waves but also applies stronger stresses closer to the ice edge, thus leading to a steeper increase in ice thickness at the ice edge creating thicker ice, which attenuates waves more strongly. By opposition, weaker attenuation applies weaker stresses over a wider region and causes a more gradual increase in thickness. This feedback could enhance the importance of other factors that influence wave attenuation such as floe size or the presence of frazil or grease ice under the visible ice floes in the MIZ. Combining multiple formulations, each dominant for different wave and ice characteristics could be a way to ensure more realistic simulations. Until then, simpler average models may provide better results, as was the case mentioned earlier.

Since waves and ice evolve in tandem, proper integration of both model components is necessary when testing models against realistic observations. As shown earlier, over the course of a few days necessary for the waves to achieve steady state, ice conditions can change significantly. Beyond improved models, further observation of waves in the MIZ, especially as the MIZ is adjusting to changing conditions, can play a pivotal role in informing the development of proper wave–ice interactions models. Specifically, open water and in-ice wave forcing along with ice thickness profiles from the ice edge would be particularly useful in validating models.

Data accessibility. The source code of the model used within this study, as well as important scripts for setup and analysis are available here: https://gitlasso.uqar.ca/jn402157/WaveIce1D.

Authors' contributions. J.A.: formal analysis, investigation, software, visualization, writing—original draft, writing—review and editing; D.D.: conceptualization, formal analysis, funding acquisition, investigation, methodology, supervision, validation, writing—review and editing; J.L.: funding acquisition, investigation, validation, writing—review and editing; H.R.: funding acquisition, investigation, project administration, resources, supervision, validation, writing—review and editing.

All authors gave final approval for publication and agreed to be held accountable for the work performed therein.

Conflict of interest declaration. The authors declare that they have no competing interests.

Funding. This research was supported by the Marine Environmental Observation, Prediction and Response (MEOPAR) Network of Centres of Excellence initial project 1.1 and contributes to the scientific programme of Québec-Océan. D.D. is funded by the National Science and Engineering Research Council (NSERC).

References

1. Wadhams P, Squire VA, Goodman DJ, Cowan AM, Moore SC. 1988 The attenuation rates of ocean waves in the marginal ice zone. *J. Geophys. Res.: Oceans* **93**, 6799–6818. (doi:10.1029/JC093iC06p06799)
2. Dumont D, Kohout A, Bertino L. 2011 A wave-based model for the marginal ice zone including a floe breaking parameterization. *J. Geophys. Res.: Oceans* **116**. (doi:10.1029/2010jc006682)
3. Wadhams P. 1983 A mechanism for the formation of ice edge bands. *J. Geophys. Res.: Oceans* **88**, 2813–2818. (doi:10.1029/JC088iC05p02813)
4. Kacimi S, Kwok R. 2022 Arctic snow depth, ice thickness and volume from ICESat-2 and CryoSat-2: 2018–2021. *Geophys. Res. Lett.* **49**, e2021GL097448. (doi:10.1029/2021GL097448)
5. Squire VA. 2020 Ocean wave interactions with sea ice: a reappraisal. *Annu. Rev. Fluid Mech.* **52**, 37–60. (doi:10.1146/annurev-fluid-010719-060301)
6. Wadhams P. 1973 Attenuation of swell by sea ice. *J. Geophys. Res.* **78**, 3552–3563. (doi:10.1029/JC078i018p03552)
7. Kohout A, Meylan M. 2008 An elastic plate model for wave attenuation and ice floe breaking in the marginal ice zone. *J. Geophys. Res.: Oceans* **113**. (doi:10.1029/2007jc004434)
8. Williams TD, Bennetts LG, Squire VA, Dumont D, Bertino L. 2013 Wave–ice interactions in the marginal ice zone. Part 1: theoretical foundations. *Ocean Model.* **71**, 81–91. (doi:10.1016/j.ocemod.2013.05.010)
9. Williams TD, Bennetts LG, Squire VA, Dumont D, Bertino L. 2013 Wave–ice interactions in the marginal ice zone. Part 2: numerical implementation and sensitivity studies along 1D transects of the ocean surface. *Ocean Model.* **71**, 92–101. (doi:10.1016/j.ocemod.2013.05.011)
10. Montiel F, Squire V, Bennetts L. 2016 Attenuation and directional spreading of ocean wave spectra in the marginal ice zone. *J. Fluid Mech.* **790**, 492–522. (doi:10.1017/jfm.2016.21)
11. Ardhuin F, Boutin G, Stopa J, Girard-Ardhuin F, Melsheimer C, Thomson J, Kohout A, Doble M, Wadhams P. 2018 Wave attenuation through an arctic marginal ice zone on October 12, 2015: 2. Numerical modeling of waves and associated ice break-up. *J. Geophys. Res.: Oceans* **123**, 5652–5668. (doi:10.1002/2018JC013784)
12. Sutherland G, Rabault J, Christensen KH, Jensen A. 2019 A two layer model for wave dissipation in sea ice. *Appl. Ocean Res.* **88**, 111–118. (doi:10.1016/j.apor.2019.03.023)
13. Voermans J, Babanin A, Thomson J, Smith M, Shen H. 2019 Wave attenuation by sea ice turbulence. *Geophys. Res. Lett.* **46**, 6796–6803. (doi:10.1029/2019GL082945)

14. Sutherland G, Rabault J. 2016 Observations of wave dispersion and attenuation in landfast ice. *J. Geophys. Res.: Oceans* **121**, 1984–1997. (doi:10.1002/2015JC011446)
15. Montiel F, Kohout AL, Roach LA. 2022 Physical drivers of ocean wave attenuation in the marginal ice zone. *J. Phys. Oceanogr.* **52**, 889–906. (doi:10.1175/JPO-D-21-0240.1)
16. Mosig JE, Montiel F, Squire VA. 2015 Comparison of viscoelastic-type models for ocean wave attenuation in ice-covered seas. *J. Geophys. Res.: Oceans* **120**, 6072–6090. (doi:10.1002/2015JC010881)
17. Lin S, Sheng J, Xing J. 2021 A comparative study of viscoelastic models for ocean wave dissipation in ice-covered regions of the Eastern Canadian shelf. *Cont. Shelf Res.* **223**, 104424. (doi:10.1016/j.csr.2021.104424)
18. Herman A. 2018 Wave-induced surge motion and collisions of sea ice floes: finite-floe-size effects. *J. Geophys. Res.: Oceans* **123**, 7472–7494. (doi:10.1029/2018JC014500)
19. Pellerin P, Ritchie H, Saucier FJ, Roy F, Desjardins S, Valin M, Lee V. 2004 Impact of a two-way coupling between an atmospheric and an ocean-ice model over the gulf of St. Lawrence. *Mon. Weather Rev.* **132**, 1379–1398. (doi:10.1175/1520-0493(2004)132<1379:IOATCB>2.0.CO;2)
20. Longuet-Higgins MS, Stewart R. 1964 Radiation stresses in water waves; a physical discussion, with applications. *Deep Sea Res. Oceanogr. Abstr.* **11**, 529–562. (doi:10.1016/0011-7471(64)90001-4)
21. Stopa JE, Sutherland P, Ardhuin F. 2018 Strong and highly variable push of ocean waves on southern ocean sea ice. *Proc. Natl Acad. Sci. USA* **115**, 5861–5865. (doi:10.1073/pnas.1802011115)
22. Williams TD, Rampal P, Bouillon S. 2017 Wave-ice interactions in the neXtSIM sea ice model. *Cryosphere Discuss.* **11**, 2117–2135. (doi:10.5194/tc-2017-24)
23. Sutherland P, Dumont D. 2018 Marginal ice zone thickness and extent due to wave radiation stress. *J. Phys. Oceanogr.* **48**, 1885–1901. (doi:10.1175/JPO-D-17-0167.1)
24. Auclair JP, Lemieux JF, Tremblay LB, Ritchie H. 2017 Implementation of Newton's method with an analytical Jacobian to solve the 1D sea ice momentum equation. *J. Comput. Phys.* **340**, 69–84. (doi:10.1016/j.jcp.2017.02.065)
25. Zhang J, Hibler III W. 1997 On an efficient numerical method for modeling sea ice dynamics. *J. Geophys. Res.: Oceans* **102**, 8691–8702. (doi:10.1029/96JC03744)
26. Hunke EC. 2001 Viscous–plastic sea ice dynamics with the EVP model: linearization issues. *J. Comput. Phys.* **170**, 18–38. (doi:10.1006/jcph.2001.6710)
27. Lipscomb WH, Hunke EC, Maslowski W, Jakacki J. 2007 Ridging, strength, and stability in high-resolution sea ice models. *J. Geophys. Res.* **112**, 18. (doi:10.1029/2005jc003355)
28. McPhee M. 1975 Ice-ocean momentum transfer for the AIDJEX ice model. *Aidjex Bull* **29**, 93–111. (doi:10.1029/92JC00239)
29. Lüpkes C, Gryanik VM, Hartmann J, Andreas EL. 2012 A parametrization, based on sea ice morphology, of the neutral atmospheric drag coefficients for weather prediction and climate models. *J. Geophys. Res.: Atmospheres* **117**. (doi:10.1029/2012jd017630)
30. Hibler III W. 1979 A dynamic thermodynamic sea ice model. *J. Phys. Oceanogr.* **9**, 815–846. (doi:10.1175/1520-0485(1979)009<0815:adtsim>2.0.co;2)
31. Lemieux JF, Tremblay B. 2009 Numerical convergence of viscous-plastic sea ice models. *J. Geophys. Res.: Oceans* **114**. (doi:10.1029/2008JC005017)
32. Kreyscher M, Harder M, Lemke P, Flato GM. 2000 Results of the sea ice model intercomparison project: evaluation of sea ice rheology schemes for use in climate simulations. *J. Geophys. Res.: Oceans* **105**, 11 299–11 320. (doi:10.1029/1999JC000016)
33. Uzuner MS, Kennedy JF. 1976 Theoretical model of river ice jams. *J. Hydraulics Div.* **102**, 1365–1383. (10.1061/JYCEAJ.0004618)
34. Dai M, Shen HH, Hopkins MA, Ackley SF. 2004 Wave rafting and the equilibrium pancake ice cover thickness. *J. Geophys. Res.: Oceans* **109**. (doi:10.1029/2003JC002192)
35. Chikhar K, Lemieux JF, Dupont F, Roy F, Smith GC, Brady M, Howell SE, Beaini R. 2019 Sensitivity of ice drift to form drag and ice strength parameterization in a coupled ice–ocean model. *Atmos. Ocean* **57**, 1–21. (doi:10.1080/07055900.2019.1694859)
36. Liu A, Mollo-Christensen E. 1988 Wave propagation in a solid ice pack. *J. Phys. Oceanogr.* **18**, 1702–1712. (doi:10.1175/1520-0485(1988)018<1702:WPIASI>2.0.CO;2)
37. Arakawa A, Lamb VR. 1977 Computational design of the basic dynamical processes of the UCLA general circulation model. *Methods Comput. Phys.* **17**, 173–265. (doi:10.1016/b978-0-12-460817-7.50009-4)

38. Lax P, Wendroff B. 1960 Systems of conservation laws. *Commun. Pure Appl. Math.* **13**, 217–237. (doi:10.1002/cpa.3160130205)
39. Sweby PK. 1984 High resolution schemes using flux limiters for hyperbolic conservation laws. *SIAM J. Numer. Anal.* **21**, 995–1011. (doi:10.1137/0721062)
40. Lemieux JF, Knoll D, Losch M, Girard C. 2014 A second-order accurate in time IMplicit-EXplicit (IMEX) integration scheme for sea ice dynamics. *J. Comput. Phys.* **263**, 375–392. (doi:10.1016/j.jcp.2014.01.010)
41. Williams J, Tremblay LB, Lemieux JF. 2017 The effects of plastic waves on the numerical convergence of the viscous–plastic and elastic–viscous–plastic sea-ice models. *J. Comput. Phys.* **340**, 519–533. (doi:10.1016/j.jcp.2017.03.048)
42. Pierson WJ, Moskowitz L. 1964 A proposed spectral form for fully developed wind seas based on the similarity theory of SA Kitaigorodskii. *J. Geophys. Res.* **69**, 5181–5190. (doi:10.1029/JZ069i024p05181)
43. Bouws E *et al.* 1998 *Guide to wave analysis and forecasting. WMO-No. 702*. Geneva, Switzerland: World Meteorological Organization.